

# 1/ $f$ Noise in Synthetic and Solar Wind Data: Superposition Principles

Jiaming Wang (王嘉明),<sup>1</sup>★ Francesco Pecora,<sup>1</sup> Rohit Chhiber,<sup>1,2</sup> Rayta A. Pradata,<sup>1</sup> Subash Adhikari,<sup>1</sup> William H. Matthaeus<sup>1</sup>

<sup>1</sup>Department of Physics and Astronomy, University of Delaware, Newark, Delaware 19716, USA

<sup>2</sup>Heliophysics Science Division, NASA Goddard Space Flight Center, Greenbelt, Maryland 20771, USA

Accepted XXX. Received YYY; in original form ZZZ

## ABSTRACT

The interplanetary magnetic field exhibits a distinctive 1/ $f$  spectral density from frequencies of around 10<sup>-6</sup> Hz to around 10<sup>-4</sup> Hz, ranging from harmonics of the solar rotation to the reciprocal of the turbulence correlation time in the spacecraft frame. Various theories have been proposed to explain its origin, typically invoking either processes in the lower corona or in the solar interior, or local interplanetary dynamics. Here, we investigate the *superposition principle* that underlies explanations of the solar/coronal types, which in principle can generate the full observed range of 1/ $f$  noise. Using synthetic time series with scale-invariant or log-normal distributions of correlation times, we examine the efficacy of several superposition approaches in generating a 1/ $f$  regime. The persistence of 1/ $f$  spectrum is further illustrated with decade-long *in situ* magnetic field measurements from the ACE spacecraft. Together, these results help explain the ubiquity of 1/ $f$  noise under the unavoidable superposition inherent in long-duration heliospheric data.

**Key words:** Heliophysics – Space plasma – Solar Dynamo

## 1 INTRODUCTION

The presence of “1/ $f$  noise”, or *flicker noise*, in the interplanetary medium is a familiar observation, while at the same time, its origin remains elusive. Generally associated with a power-law spectral density in the frequency  $f$  domain, this phenomenon often spans more than a decade in scale. At 1 au, 1/ $f$  signals have been observed in fluctuations of the magnetic field (Matthaeus & Goldstein 1986; Feynman & Ruzmaikin 1994) and in the plasma density (Matthaeus et al. 2007). 1/ $f$  noise in magnetic field persists into the inner heliosphere as indicated by measurements from MESSENGER and the Parker Solar Probe (Davis et al. 2023; Huang et al. 2023; Pradata et al. 2025; Huang et al. 2025). Beyond *in situ* measurements, 1/ $f$  noise has been identified in remote sensing data using line of sight photospheric magnetic field (Nakagawa & Levine 1974; Matthaeus et al. 2008) and inferred in channel-integrated SOHO/UVCS data (Bemporad et al. 2008). NASA’s Parker Solar Probe (PSP) Science and Technology Definition team identified the potential discovery of the origin of the interplanetary 1/ $f$  signal as a major goal for the PSP mission (McComas & others 2008).

Discussions of the origin of 1/ $f$  noise in the interplanetary medium may be roughly divided into two classes: those attributing it to local *in situ* dynamical processes, and those linking it to remote activities, perhaps in the sub-Alfvénic corona or even within the solar interior beneath the photosphere. This paper sets its context in the latter category, hereafter referred to as the *solar origin* for brevity.

Beyond the solar wind, a great variety of other systems also display 1/ $f$  signature (see, e.g., review by Dutta & Horn 1981; Wang et al. 2024a), rendering it a subject of considerable study across disciplines. Of particular interest for broad applicability are the suggestions of generic principles that can be responsible for producing a 1/ $f$  signal but do not require specific dynamical mechanisms. Generic principles include the superposition principle that will be the main subject here as initially described by Van Der Ziel (1950) and Machlup (1981), as well as ideas based on self-organized criticality (SOC) phenomenon, including the “sandpile” models (see, e.g., Bak et al. 1987; Hwa & Kardar 1992; Consolini et al. 2015; Korzeniowska et al. 2023). There has been substantial discussion in the literature regarding possible relationships or distinctions between these two general classes (see, e.g., Bruno & Carbone 2013; Lamarre et al. 2025). Other models for generating scale-invariant signals either in time (to obtain 1/ $f$  in frequency) or in space (1/ $k$  in wavenumber  $k$ ) have been discussed, often in the context of self organization or inverse cascade. These phenomena are typically slow, requiring many nominal nonlinear times (Brandenburg 2001; Dmitruk & Matthaeus 2007; Dmitruk et al. 2011). There are also models that invoke local processes or instabilities, and some balance between spectral transfer and expansion (Velli et al. 1989; Huang et al. 2023, 2025). Such local models may be self-consistent, but are intrinsically limited in their range of influence. That is, they may not be able to explain very low-frequency spectra due to limited solar wind propagation time (Zhou et al. 1990; Chhiber 2018).

The main purpose here is to examine in some detail the nature of signal superposition as an explanation for the generation of 1/ $f$  noise in a system such as the solar wind. The widely quoted superpo-

★ E-mail: jmwang@udel.edu

sition ideas of [Van Der Ziel \(1950\)](#) and [Machlup \(1981\)](#), along with enabling frequent appearance of log-normal distributions of relevant physical quantities ([Montroll & Shlesinger 1982](#)), are couched in applied mathematical terms. Usual descriptions involve superposed exponential correlation functions and associated spectra, as briefly outlined in the following section. However, the application of superposition to the underlying physical data is rarely explicated in any detail, even if it appears to be reasonable on an intuitive level. Therefore, this paper focuses on examination of several versions of superposition in the time domain, as described in the following sections.

In the solar wind and coronal context, superposition might involve successive magnetic flux tube merging that creates a log-normal distribution of correlation scales ([Matthaeus & Goldstein 1986](#)). Recently, log-normal correlation scales have been observed in the solar photosphere and the low corona ([Sharma & Morton 2023](#); [Chhiber et al. 2025](#)). The requisite large scales as indicated by the low-frequency extent of the observed interplanetary  $1/f$  band may also be linked to processes in the solar dynamo, as motivated by dynamo simulations and experiments ([Ponty et al. 2004](#); [Dmitruk et al. 2014](#)). Or they may be linked to inverse cascade systems known to produce timescales much greater than the band-limited scales of the system ([Dmitruk & Matthaeus 2007](#); [Dmitruk et al. 2011](#)). In this regard, the limitation on available dynamical timescales could be alleviated, given that the relevant mechanisms operate in sub-Alfvénic coronal regions, where a parcel of plasma may reside for many nonlinear times, rather than in the super-Alfvénic wind.

Here, we do not attempt detailed explanation of the exact mechanism that creates the log-normal distribution underlying the superposition procedure, but look at different ways signals may be superposed and their effectiveness in generating  $1/f$  noise, without prejudice concerning the location at which this occurs. The paper is organized as follows. In the next section, we describe the fundamental superposition principle. In Section 3, several versions of superposition are described and analyzed in the context of synthetic datasets, with details of their construction provided in the Appendix. In Section 4, these superposition versions are studied employing a 12-year ACE dataset at 1 au. Section 5 summarizes and discusses the results.

## 2 OVERVIEW OF THE SUPERPOSITION PRINCIPLE

It has been demonstrated by [Machlup \(1981\)](#) that the superposition of “purely random” processes – defined as those with exponentially decaying autocorrelations of the form  $e^{-\tau/\tau_c}$  where  $\tau_c$  is the characteristic correlation time – results in a  $1/f$  power spectrum, provided that the ensemble of  $\tau_c$  follows a scale-invariant distribution. The autocorrelation function of a zero-mean time series  $x(t)$  can be defined as  $R(\tau) = \langle x(t)x(t+\tau) \rangle$ , where  $\tau$  represents the time lag. Then, the Fourier transform of a single exponential autocorrelation function  $R(\tau_c, \tau) \propto e^{-\tau/\tau_c}$  in angular frequency ( $\omega = 2\pi f$ ) domain yields a spectrum of Lorentzian form:

$$S(\tau_c, \omega) = \int_{-\infty}^{\infty} e^{-i\omega\tau} R(\tau_c, \tau) d\tau \propto \frac{2\langle x^2 \rangle \tau_c}{1 + \tau_c^2 \omega^2}, \quad (1)$$

where  $R(\tau)$  is an even function symmetric about the origin, assuming the homogeneity of the data. Hereafter, we will assume a unit variance  $\langle x^2 \rangle = 1$  unless otherwise specified. When multiple spectra of equal integrated power are superposed under the assumption that  $\tau_c$  follows an inverse (scale-invariant) distribution  $\rho(\tau_c) d\tau_c \propto d\tau_c / \tau_c$  within

some specified domain  $[\tau_1, \tau_2]$ , the resulting overall spectrum is

$$\langle S(\omega) \rangle = \int_{\tau_1}^{\tau_2} S(\tau_c, \omega) \rho(\tau_c) d\tau_c \propto \frac{\tan^{-1}(\tau_c \omega)}{\omega} \Big|_{\tau_c=\tau_1}^{\tau_2}. \quad (2)$$

Assuming  $\tau_1 \ll \tau_2$ , and within the frequency range where  $1/\tau_2 \ll \omega \ll 1/\tau_1$ , Eq. 2 leads to

$$\langle S(\omega) \rangle \propto \frac{\frac{\pi}{2} + O(\frac{1}{\tau_2 \omega}) - O(\tau_1 \omega)}{\omega}. \quad (3)$$

Thus under zeroth-order approximation,  $\langle S \rangle \propto 1/\omega$  where  $1/\tau_2 \ll \omega \ll 1/\tau_1$ .

This argument is often interpreted to suggest that scale-invariant phenomena arise from processes lacking a characteristic scale. The extent of the  $1/f$  spectrum is directly related to the span of timescales.

[Montroll & Shlesinger \(1982\)](#) later pointed out that an inverse distribution is not normalizable without imposing lower and upper bounds, which may be unrealistic in many natural systems lacking sharp boundaries, including the solar wind. A log-normal distribution with sufficiently large variance has been proposed as a suitable substitution. Adopting the condition in [Wang et al. \(2024a\)](#) that a log-normal random variable  $x \sim \text{logNormal}(\mu, \sigma^2)$  within the domain such that  $|\ln(x/\bar{x})| \leq \sqrt{2\theta\sigma^2}$ , where  $\bar{x} \equiv e^\mu$ , is scale-invariant within a factor of tolerable deviation  $\theta$ , then the boundaries of the scale-invariant portion are  $\exp(\mu \pm \sqrt{2\theta\sigma^2})$ . In this simplistic perspective, the  $1/f$  regime spans for approximately a factor of  $\exp(2\sqrt{2\theta\sigma^2})$ , independent of  $\mu$ . The correlation time at 1 au is log-normal with the variance of the underlying normal distribution being around unity (see Section 4, also see [Ruiz et al. \(2014\)](#)). A  $\theta$  value of 0.5 would then yield nearly three-quarters of a decade of  $1/f$  range in the solar wind spectrum.<sup>1</sup>

While Machlup’s  $1/f$  model is broadly relevant, the solar wind turbulence spectra are often not Lorentzian as in Eq. 1. For example, isotropic and incompressible hydrodynamic turbulence in the inertial range acquires the Kolmogorov  $k^{-5/3}$  power-law scaling, which is frequently observed as  $f^{-5/3}$  in time domain in the interplanetary spectrum (see, e.g., review by [Bruno & Carbone 2013](#)). Toward lower heliocentric distances with increasing magnetic field strength, inertial range spectrum shifts to a near  $f^{-3/2}$  scaling (see, e.g., recent work by [Chen et al. 2020](#); [Davis et al. 2023](#)) consistent with the classical theory of magnetohydrodynamic (MHD) turbulence ([Biskamp 2003](#)). In [Wang et al. \(2024a\)](#), we state a generalized version of the aforementioned superposition principle, in which the  $1/f$  noise emerges from superposing power-laws of arbitrary index less than  $-1$ , thereby justifying the applicability of the superposition principle in the solar wind. In the next section, we generate time series with  $f^{-5/3}$  power-laws to test the robustness of the superposition principle.

## 3 SUPERPOSITION WITH SYNTHETIC DATA

The term “superposition” in the [Machlup \(1981\)](#) model refers specifically to taking the ensemble mean of the spectra, or equivalently, the correlations. This procedure does not correspond in any obvious way to the physical processes occurring in the solar wind, or how the relevant quantities are measured by spacecraft instruments – that

<sup>1</sup> The observed interplanetary  $1/f$  band extends over more than a decade down to  $10^{-6}$  Hz, which implies the presence of correlations on timescales substantially longer than the local turbulence correlation time typically inferred from the  $1/e$  method in the literature and considered here (see Section 4).

is, the solar wind does not superpose correlation functions. On the other hand, while it is clear that signals themselves (e.g. the magnetic fields) are superposed either in generation or in transport, the exact nature or even the location of the superposition has not so far been established. Long-duration measurements necessarily include plasma patches originating from a range of solar latitudes and longitudes, being then deflected and mixed during their transport through the heliosphere (see, e.g., Levine et al. 1977; Servidio et al. 2014; Chhiber et al. 2021). Consequently, samples widely separated in time and recorded by a single spacecraft are essentially uncorrelated with regard to their details, even if they broadly share statistical variations of their common source in the solar interior or dynamo. Additionally, wind streams from a fixed location on the solar surface can still vary in source and composition over timescales of several days, partly because the ubiquitous magnetic carpet is dynamically replaced on around 40-hour timescales (Priest et al. 2002). Therefore, given the need of month- to year-long intervals to capture the full bandwidth of heliospheric  $1/f$  noise (as discussed in Section 1), some form of superposition in the 1 au dataset is unavoidable.

To bridge the analytical model and observational practice, we explore in this section four methods of superposition using synthetic time series:

- (i) averaging the correlation functions,
- (ii) averaging the time series,
- (iii) concatenating the collection of time series, and
- (iv) truncating each time series to a random (uniformly distributed) length between one and one-twentieth of the interval duration, then concatenating the truncated segments.

Note that method 1 aligns with Machlup's procedure. Different methods may capture different aspects of solar wind dynamics, depending on the nature of the underlying variability that generates approximate scale-invariance or log-normality.

### 3.1 Generation of synthetic time series

We create 500 sets of random time series, each having  $N = 1440$  data points to mimic a 1-day dataset with 1-minute resolution, and each with a mean of zero and a variance of unity. Each time series is specified with a characteristic correlation time  $\tau_c = 1/f_{\text{break}}$ , where  $f_{\text{break}}$  is an onset frequency below which the spectrum is flat and above which the spectrum has a  $f^{-5/3}$  scaling. The collection of  $\tau_c$  values follows a scale-invariant (or inverse) distribution of the form

$$\rho(\tau_c)d\tau_c = \frac{d\tau_c}{\tau_c \ln(\tau_2/\tau_1)}, \quad (4)$$

where  $\tau_c$  spans from  $\tau_1$  to  $\tau_2$ . From Eq. 3,  $1/f$  band in the superposed data is expected to span from several factors above  $1/2\pi\tau_2$  to several factors below  $1/2\pi\tau_1$  in frequency space. We also analyze time series generated from the overlapping log-normal distribution, with parameters  $\mu \approx [\ln(\tau_1\tau_2)]/2$  and  $\sigma^2 \approx [\ln(\tau_2/\tau_1)]^2/8\theta$ .

A time series  $x_j$ ,  $j = 0, \dots, N-1$ , is generated using the familiar procedure of (1) specifying a power spectrum  $S_m$ ; (2) using the power spectrum to determine the Fourier amplitudes  $X_m$  of the target data and then randomizing its phases; and (3) arriving at the time series through inverse Fourier transform. The procedure is described in detail in Appendix A.

Since the generation and analysis of the synthetic data are independent of the value of the time resolution  $\Delta t$ , we normalize all variables by  $\Delta t$ . This yields dimensionless variables (represented by overline notation)  $\overline{\Delta t} = 1$ ,  $\overline{t} = t/\Delta t$ ,  $\overline{f} = f\Delta t$ ,  $\overline{S}_m = S_m/\Delta t$ , and  $\overline{X}_m = X_m/\Delta t$ . For simplicity, we carry out this normalization and omit the overline notation from this point onward unless stated otherwise.

We present results for three distributions of  $\tau_c$ : (i) inverse distribution with  $\tau_1, \tau_2 = 3, 150$  to show an extended  $1/f$  range for clear comparison of four methods of superposition; (ii) inverse distribution with  $\tau_1, \tau_2 = 20, 150$  to mirror 1 au correlation times in minutes (see Fig. 4 or Ruiz et al. (2014)); and (iii) log-normal distribution with  $\mu, \sigma^2 = 4, 1$  with a scale-invariant portion that overlaps approximately with distribution (ii) employing  $\theta = 0.5$ . For case (i), the minimum break frequency is  $1/\tau_2 \approx 7 \times 10^{-3}$ , which is sufficiently greater than the frequency resolution of  $\Delta f = 1/N \approx 7 \times 10^{-4}$ , so that the smallest frequency break can be resolved.

### 3.2 Analysis of synthetic time series

Having obtained the synthetic time series, the normalized two-point correlation function, defined as

$$R_j = \frac{\langle x_i x_{i+j} \rangle - \langle x_i \rangle \langle x_{i+j} \rangle}{\langle x_i^2 \rangle - \langle x_i \rangle^2}, \quad (5)$$

is computed using the Blackman-Tukey algorithm (Blackman & Tukey 1958; Matthaeus & Goldstein 1982b). Note that the normalization as in the denominator is redundant for data with unit variance. The operation  $\langle \dots \rangle$  denotes ensemble expectation, which is implemented in practice as averaging over the data domain indexed by  $i$  (see details in Wang et al. 2024b). The lag index  $j$  ranges from 0 to 30% of the duration of  $x_j$ . For individual time series, this covers nearly three times the maximum correlation time while maintaining an adequate statistical weight for each correlation value. For stationary data, the correlation value is independent of shifts in the index  $i$ , that is, independent of the origin of time (Matthaeus & Goldstein 1982b).

The power spectral density  $S(f)$  is defined as the Fourier transform of the symmetrized correlation function. Operationally, since the correlation function is obtained on a discrete grid, the spectrum is discretized as

$$S_m = \sum_{j=0}^{2M-1} e^{-i2\pi m j / 2M} R_j, \quad (6)$$

where  $M = 432$  (30% of the 1440 data points), and  $R_{2M-j} = R_j$  for  $j = M+1, \dots, 2M-1$ . It can be shown that Eq. 6 is equivalent to

$$S_m = \sum_{j=-M}^{M-1} e^{-i2\pi m j / 2M} R_j, \quad (7)$$

where  $R_j = R_{-j}$ . We choose Eq. 6 for convenience in numerical implementation.

To prevent  $R_j$  from being artificially treated as periodic over the finite domain  $[-N, N]$ , we first apply a 10% cosine-taper window, as described in Wang et al. (2024b). We then extend the correlation function by zero-padding its tail, imitating an infinite domain (Matthaeus & Goldstein 1982b). The tapering and zero-padding procedures reduce spectral noise at high frequencies approaching the maximally resolved (Nyquist) frequency. This procedure has negligible impact on the shape of the spectrum within the range of interest (not shown).

The spectra produced by methods 2, 3, and 4 necessarily show substantial fluctuations. To examine the spectral shape underlying these statistical fluctuations, we apply a moving-average filter iteratively 10 times. At each iteration, the value of  $S_m$  is updated to  $0.5S_m + 0.25(S_{m-1} + S_{m+1})$  (Matthaeus & Goldstein 1982b).

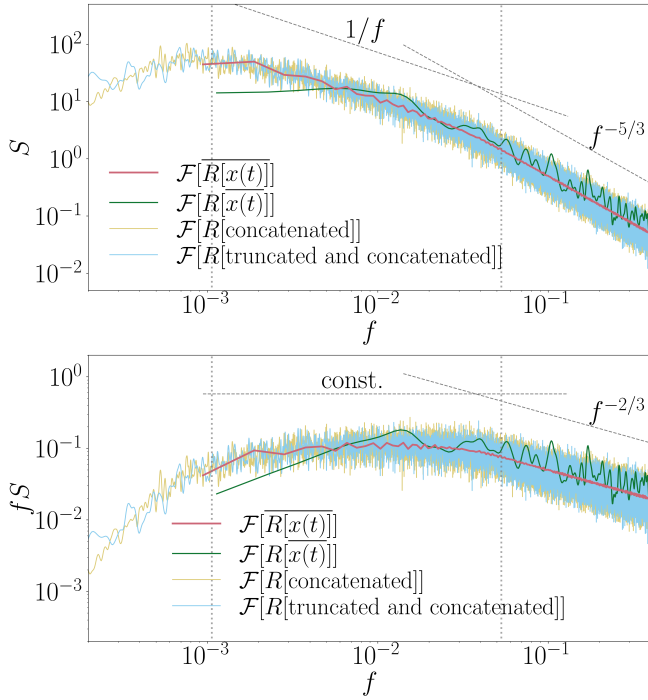


**Figure 1.** Top panel: power spectra resulting from scale-invariant correlation times with  $\tau_1, \tau_2 = 3, 150$ , obtained through superposition methods 1 (in red), 2 (in green), 3 (in yellow), and 4 (in blue). Bottom panel: compensated spectra corresponding to those on top panel. Dotted vertical lines mark frequencies  $1/2\pi\tau$  associated with the minimum and maximum correlation times, respectively. Dashed gray lines are guiding power-laws with index  $-1$  and  $-5/3$ , respectively.

### 3.3 Results

For a correlation time distribution of type (i) with  $\tau_1, \tau_2 = 3, 150$ , the top panel of Fig. 1 illustrates the spectra resulting from the different superposition methods. Method 1, averaging the correlation functions (labeled as  $\mathcal{F}[R[x(t)]]$ ), has spectrum retaining the  $-5/3$  power-law index at frequencies  $f \gg 1/2\pi\tau_1$ , and gradually transitions to a  $-1$  index at lower frequencies. At even lower frequencies where  $f \sim 1/2\pi\tau_2$ , the spectrum flattens before being affected by the limited frequency resolution. The frequencies at  $1/2\pi\tau_1$  and  $1/2\pi\tau_2$  are indicated by dotted vertical lines.

In contrast, Method 2 – averaging the time series (labeled as  $\mathcal{F}[R[\overline{x}(t)]]$ ) – exhibits no discernible  $1/f$  band, showing only a weak spectral shallowing before the transition to the uncorrelated flat band. Agreement between Methods 1 and 2 is generally not expected, as it would require the ensemble of time series  $\{x(t)\}$  to satisfy  $\langle \overline{x}(t)x(t+\tau) \rangle \sim \langle \overline{x}(t)\overline{x}(t+\tau) \rangle$ , where  $\langle \dots \rangle$  denotes an ensemble (inter-series) average and  $\overline{\dots}$  denotes a temporal (intra-series) average. An equivalence would imply the convergence of cross-correlation between datasets to autocorrelation and, ultimately, self-averaging of the ensemble. Or it would simply imply an absence of cross-correlation. Neither properties is enforced here.

The superposed spectra resulting from Method 3 (concatenating the time series) and Method 4 (truncating each time series before concatenation) are also shown in the top panel of Fig. 1. Despite enhanced fluctuations from long sample duration, both methods produce spectral shapes consistent with those from Method 1. Comparing Methods 3 and 4 shows that arbitrary truncation has minimal impact on the superposed spectrum, in both the  $1/f$  and the  $f^{-5/3}$

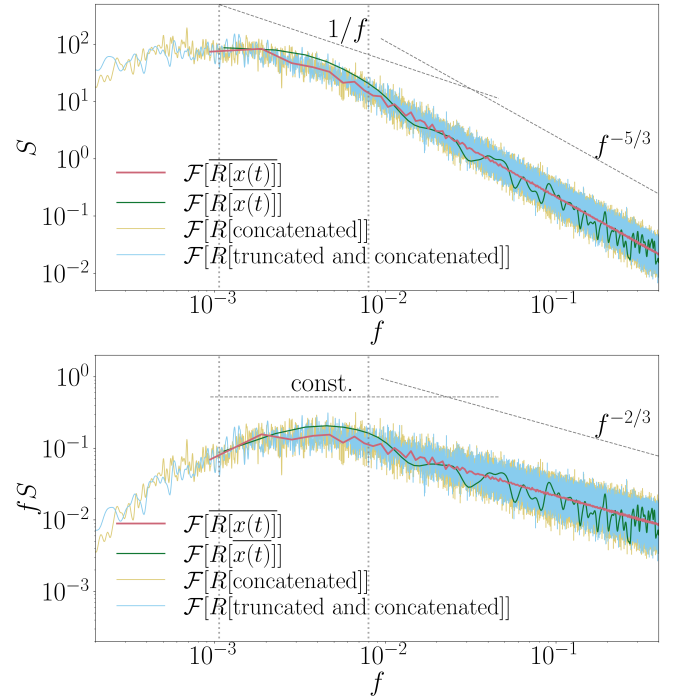


**Figure 2.** Top panel: power spectra resulting from scale-invariant correlation times with  $\tau_1, \tau_2 = 20, 150$ , obtained through superposition methods 1 (in red), 2 (in green), 3 (in yellow), and 4 (in blue). Bottom panel: compensated spectra corresponding to those on top panel. Dotted vertical lines mark frequencies  $1/2\pi\tau$  associated with the minimum and maximum correlation times, respectively. Dashed gray lines are guiding power-laws with index  $-1$  and  $-5/3$ , respectively.

bands where  $f \gg 1/2\pi\tau_2$ , even when some segment durations are shorter than their characteristic correlation times. Additionally, varying the lower bound of the possible truncation range from 20% to 1% of the 1440 data points results in no detectable change in the spectral shape (not shown). This finding is particularly relevant to spacecraft measurements, suggesting that  $1/f$  signals can be recovered even when data gaps or irregular sampling renders some intervals highly fragmented. To highlight the emergence of a  $1/f$  regime, we show the corresponding compensated spectra from the four methods in the bottom panel of Fig. 1.

Figs. 2 and 3 show results for correlation time distributions of type (ii) with  $\tau_1, \tau_2 = 20, 150$  and of type (iii) with  $\mu, \sigma^2 = 4, 1$ , respectively. These choices are intended to resemble the distributions observed in the 1 au solar wind, as will be shown in Fig. 4 in Section 4. Overall, the spectral behavior is similar to that of the type (i) distribution case, with clear  $1/f$  band appearing between the low-frequency flat band associated with uncorrelated fluctuations and the high-frequency  $f^{-5/3}$  band. For the log-normal distribution case (Fig. 3), the dotted vertical lines mark the boundaries  $\exp(\mu \pm \sqrt{2\theta\sigma^2})$  of the scale-invariant region assuming a tolerable deviation factor of  $\theta = 0.5$ . As predicted, despite more gradual spectral transitions on both sides as compared to the type (ii) case, a distinct  $1/f$  band still emerges between these boundaries for superposition Methods 1, 3, and 4.

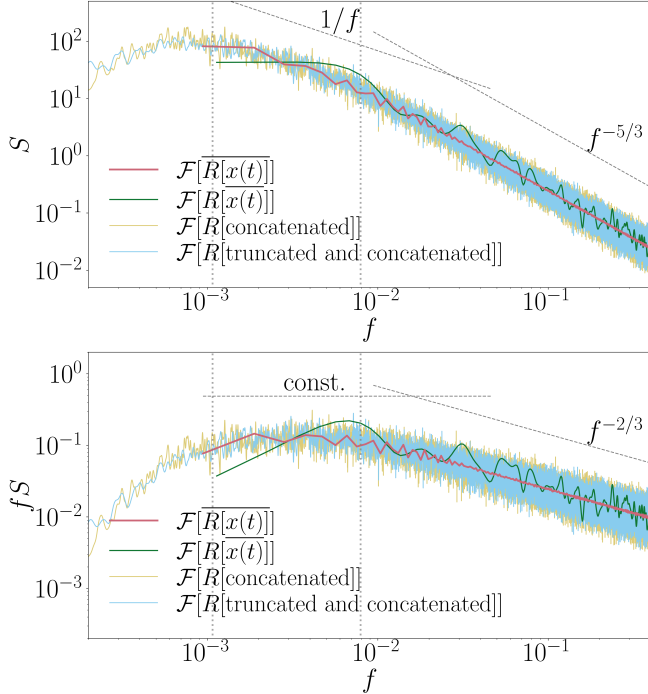


**Figure 3.** Top panel: power spectra resulting from log-normal correlation times with  $\mu$ ,  $\sigma^2 = 4, 1$ , obtained through superposition methods 1 (in red), 2 (in green), 3 (in yellow), and 4 (in blue). Bottom panel: compensated spectra corresponding to those on top panel. Dotted vertical lines mark  $2\pi$ -scaled boundaries of scale-invariant correlation time portion with  $\theta = 0.5$  (see text). Dashed gray lines are guiding power-laws with index  $-1$  and  $-5/3$ , respectively.

#### 4 SUPERPOSITION WITH 1 AU OBSERVATION

In the previous sections, we emphasized a generic mechanism for generating  $1/f$  noise through an ensemble of signals. While not of the  $1/f$ -type in isolated samples, these signals collectively give rise to a  $1/f$  spectrum. Assuming this procedure underlies the emergence of  $1/f$  noise in the solar wind, a natural question is whether we can directly observe the process of  $1/f$  formation at 1 au. As argued earlier, this is not feasible, as signals almost certainly already have undergone superposition of some form beginning at the base of the solar wind. However, by partitioning a long data record into subsets and comparing the resulting spectra from Methods 1, 2, and 3, we can assess how well the  $1/f$  scaling is preserved (rather than created) under the superposition operation. Method 4 is redundant with respect to Method 3 in observational data, so we do not report its result.

It should be made clear that the essential distinction between the synthetic time series in Section 3 and those measured at 1 au is that the latter may incorporate multiple correlated signals (thus timescales) within a single interval. And there may be long-range effects such as the solar rotation that render correlations across separate intervals. It is thus impossible to isolate an ensemble of purely uncorrelated wind streams, which is only feasible in the realm of synthetic data. The superposition of a long-record low-frequency spectrum (Method 3) by averaging spectra from shorter subsets of naturally occurring data may produce results that deviate in subtle ways from conclusions based on our idealized model.

#### 4.1 Magnetic field data and analysis procedure

The observational dataset chosen as the testing ground for this study are magnetic field measurements at 1 au from NASA’s Advanced Composition Explorer (ACE) spacecraft (Stone et al. 1998). We analyze 12 years of data spanning from 5 February 1998 to 31 December 2009, with records from midnight to midnight in Coordinated Universal Time (UTC), covering the minimum-to-minimum phase of the 23rd solar cycle (Hathaway 2015). Since our goal is to probe the  $1/f$  range at frequencies below the nominal inertial scales, the original 1-second resolution data collected by the Magnetometer (MAG; Smith et al. 1998) aboard ACE are downsampled to 1-minute cadence, with missing values flagged as ‘NAN’. No data gap interpolation is performed. The power spectrum of this 12-year dataset has previously been analyzed in Wang et al. (2026) and shows clear  $1/f$  scaling in the trace from approximately  $4 \times 10^7$  Hz (around the solar rotation frequency) to approximately  $2 \times 10^5$  Hz. We interpret this spectrum as reflecting superposition Method 3 and use it as a reference for comparison with spectra produced from Methods 1 and 2.

For the analysis, we partition the dataset independently into two subsets, one consisting of 1-day segments and the other of 10-day segments. A segment is excluded if more than 50% of the measurements are missing. No distinction is made between segments dominated by fast or slow solar wind, nor are events such as interplanetary coronal mass ejections (ICMEs) or heliospheric current sheet (HCS) crossings removed. This is because the proposed reason of  $1/f$  emergence involves the occurrences of rare events (at the tail of the scale-invariant or log-normal distributions) – or mixtures of them – each contributing correlated signals. This results in a total of 4259 1-day intervals and 426 10-day intervals. The former set is used to estimate the interplanetary turbulence correlation time distribution, and both sets are used to reconstruct the 12-year spectrum.

For Method 1, component-wise magnetic fluctuation autocorrelations for each interval are first computed as in the numerator of Eq. 5 through the Blackman-Tukey algorithm (Blackman & Tukey 1958; Matthaeus & Goldstein 1982a), which are then summed to get the trace. As in the test with synthetic data,  $j$  indexes temporal lag  $\tau_j = j\Delta t$ ,  $\Delta t = 60$  s, and ranges from 0 to 30% of the segment duration. The magnetic spectrum is computed from the correlation through the same procedure adopted for the synthetic data, following Eq. 6 and then cosine-tapering and zero-padding. In the next subsection, we compare the “averaged-then-normalized” trace spectrum with the “normalized-then-averaged” one to see whether  $1/f$  emerging from superposition withstands variation in fluctuation variance. We repeat the analysis for 50 randomly selected 10-day intervals separated in time, thereby reducing cross-interval correlations.

For Method 2, the magnetic field measurements are averaged across all 10-day intervals to produce a single representative 10-day time series. The correlation trace of the fluctuation and the corresponding spectrum are then computed from this averaged dataset.

The turbulence correlation time is determined from the 1-day intervals as the  $e$ -folding time of the correlation trace  $R$ , i.e., the time lag where the correlation decreases by a factor of  $1/e$ . The correlation trace is first smoothed 3 times through the moving-average filter (as described in Section 3.2) to mitigate fluctuations. If the correlation does not reach the  $1/e$  level within the first 90% of its domain, we perform linear fit to  $\ln R$  versus  $\tau$  for the first 50% of the correlation to acquire the value of  $\tau$  where  $\ln R/\ln R(0) = -1$ , similar to the approach in Isaacs et al. (2015).

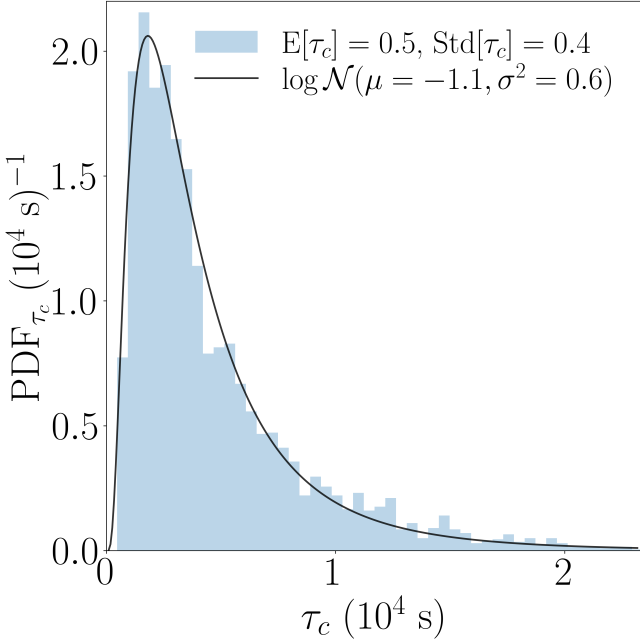


**Figure 4.** Distribution of magnetic field correlation time evaluated from 24-hour intervals. Ensemble expectation value (E) and standard deviation (Std) are listed in legend. Solid curve represents best-fit log-normal distribution with parameters also reported in legend.

## 4.2 Results

We show in Fig. 4 the distribution of magnetic field correlation times at 1 au. The correlation times follow a log-normal distribution, consistent with previous findings (Ruiz et al. 2014; Isaacs et al. 2015; Cuesta et al. 2022). Moreover, Isaacs et al. (2015) reported that both the mean and variance of this distribution increase with the duration of the averaging interval, with the trend qualitatively leading to the distribution shown in Fig. 4, obtained using 24-hour intervals. We emphasize that the  $1/e$  method employed here yields the local turbulence correlation time. Correlations on day-long and longer timescales, which may also contribute to the formation of  $1/f$  noise, are not represented in Fig. 4.

Fig. 5 shows the frequency-compensated spectra  $fS$  obtained from superposition Methods 1, 2, and 3 using ACE data. For completeness, we present the spectrum from the unsegmented 12-year time series (Method 3), as published in Wang et al. (2026), alongside our new results: the raw spectrum is smoothed 50 times and shown in gray; the frequency-integrated spectrum and its associated uncertainty are shown in blue. We show four spectra derived from averaging correlations (Method 1): the averaged-then-normalized (normalized-then-averaged) spectrum from the full set of 10-day intervals is shown in red (purple), multiplied by a factor of 2 for visualization; the averaged-then-normalized spectrum from randomly selected 10-day intervals is shown in green, multiplied by a factor of 0.5; the averaged-then-normalized spectrum from the full set of 1-day intervals is smoothed one time to suppress low-frequency fluctuations and is shown in orange. The spectrum from averaged 10-day time series (Method 2) is smoothed 10 times and shown in black.

All spectra in Fig. 5 exhibit broadly similar shapes across their overlapping frequency domains and consistently display clear  $1/f$  behavior. The presence of the Method 2 spectrum (black) within this consensus – unlike in the synthetic tests – likely reflects the

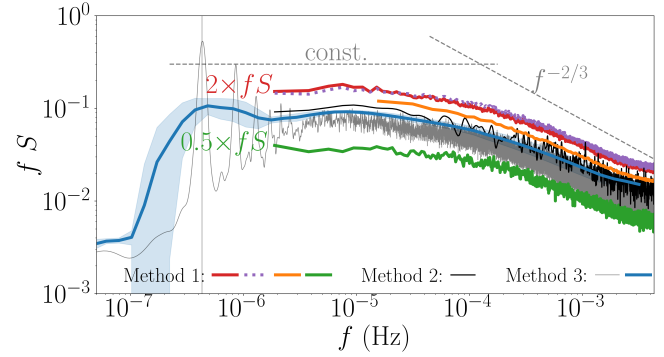


**Figure 5.** Recovery of  $1/f$  with different superposition methods. Method 1: Averaged-then-normalized spectrum from 10-day intervals (red); normalized-then-averaged spectrum (dotted purple); averaged-then-normalized spectrum from randomly selected 10-day intervals (green); averaged-then-normalized spectrum from 1-day intervals (orange). Method 2: Spectrum from averaged 10-day intervals (black). Method 3: Spectrum from unsegmented 12-year data (gray); integrated spectrum and associated uncertainty from 12-year data (blue curve and shaded area, respectively, from Wang et al. 2026). Dashed lines indicate constant and  $f^{-2/3}$  power-laws. Vertical line indicates 27-day solar rotation frequency.

relatively negligible cross-interval correlations compared to the autocorrelations within individual 10-day intervals. This is in accord with the observation that solar wind magnetic field correlations rarely return to the  $1/e$  level after de-correlating on several-hour timescales, even accounting for the moderate correlation increase at timescales associated with the solar rotation (Wang et al. 2026).

The averaged-then-normalized spectrum (red) closely matches the normalized-then-averaged spectrum (purple), indicating that the emergence of a  $1/f$  band is not sensitive to the variation in fluctuation power  $\langle x^2 \rangle - \langle x \rangle^2$  in the 10-day dataset, even though this quantity is known to follow log-normal distributions (Ruiz et al. 2014; Isaacs et al. 2015; Sharma & Morton 2023; Chhiber et al. 2025).

## 5 CONCLUSION AND DISCUSSION

Based on the generic framework of the superposition principle, we report the generation and preservation of  $1/f$  signals through four types of superposition operations: (1) averaging correlation functions, (2) averaging time series, (3) concatenating time series, and (4) concatenating randomly truncated time series. Methods 1 and 3 display very similar spectral shape in the synthetic and the measured 1 au data respectively, which is expected as data elongation translates directly to averaging the autocorrelations within the shared frequency domain. Spectral similarity between Methods 3 and 4 may reflect the fact that the correlation time is characteristic to an interval and is barely affected by interval truncation. These results are relevant to spectral analysis of observational data, as long-duration heliospheric measurements inherently consist of a mixture of signals with broadly-distributed correlation scales, and are often subject to truncation or concatenation during data collection and analysis.

The observed  $1/f$  band in Fig. 5 approximately overlaps with the range expected from the local turbulence correlation times in Fig. 4. But it extends to frequencies as low as  $10^{-6}$  Hz, comparable to the superharmonics of the solar rotation period. This indicates that long-range correlations on day- to month-timescales play a significant role in shaping the  $1/f$  spectrum. Such long correlation times cannot be captured from the conventionally used  $1/e$  method, nor can they be

estimated via correlation integration (Matthaeus et al. 2005), since the trace of the magnetic correlation oscillates around zero with solar-rotation periodicities (Matthaeus & Goldstein 1982b; Wang et al. 2026) and is therefore not integrable. We defer a detailed treatment of long-range scales to future work.

Superposition mechanisms of the type covered in the above sections are unlikely to operate locally in the super-Alfvénic wind to produce the observed interplanetary  $1/f$  signal. This assertion is based on the realization that any proposed local  $1/f$  generation mechanism faces causality and range-of-influence issues, and is not able to explain  $1/f$  behavior down to the lowest observed  $10^{-6}$  Hz frequency range (see e.g. Zhou et al. 1990; Chhiber 2018; Wang et al. 2024a). Conversely, presently available evidence points to a source of the constituents of the  $1/f$  magnetic field signal that lies deep within the corona or beneath the photosphere (Matthaeus & Goldstein 1986; Zhou et al. 1990; Wang et al. 2026). Theoretical attention then necessarily turns to identification of the responsible dynamical mechanisms. While specific inquiries along these lines are deferred to future studies, it seems likely that explanations might be developed based on dynamo theory (Moffatt 1969), self-organized criticality (Bak et al. 1988), and inverse cascade (Frisch et al. 1975). Indeed, connections between these frameworks and  $1/f$  noise are already present in the literature (Ponty et al. 2004; Dmitruk & Matthaeus 2007; Dmitruk et al. 2011, 2014; Lamarre et al. 2025).

Exploring  $1/f$  magnetic field fluctuation in the context of these frameworks is an important direction for future study. The ultra-low frequency variations that comprise the  $1/f$  signal provide a physical context and background in which extreme interplanetary events and space weather occur, thus providing substantial motivation. Future investigations may benefit from appeal to the superposition principles set out in the present series of exercises. In particular, it may be possible to characterize the relevant superposed real-space structures by analysis of imaging data from the PUNCH mission (Deforest et al. 2022), or based on statistical analysis of multi-spacecraft data from HelioSwarm (Klein et al. 2023) or the L1 constellation of spacecraft, including the IMAP mission, near 1 au (McComas et al. 2025).

## ACKNOWLEDGEMENTS

This research is partially supported by the U.S. National Science Foundation, award PHY-2108834, through the NSF/DOE Partnership in Basic Plasma Science and Engineering, by NASA LWS grants 80NSSC20K0377 (subcontract 655-001) and 80NSSC22K1020, by the NASA IMAP project at UD under subcontract SUB0000317 from Princeton University, by the NASA/SWRI PUNCH subcontract N99054DS at the University of Delaware, and by the NASA HSR grant 80NSSC18K1648.

## DATA AVAILABILITY

All study data are included in the article. There are no new observational data generated or analyzed in support of this research.

## REFERENCES

Bak P., Tang C., Wiesenfeld K., 1987, *Phys. Rev. Lett.*, **59**, 381  
 Bak P., Tang C., Wiesenfeld K., 1988, *Phys. Rev. A*, **38**, 364  
 Bemporad A., Matthaeus W. H., Poletto G., 2008, *ApJ*, **677**, L137  
 Biskamp D., 2003, Magnetohydrodynamic Turbulence. Cambridge University Press

Blackman R. B., Tukey J. W., 1958, The Measurement of Power Spectra. Dover

Brandenburg A., 2001, *ApJ*, **550**, 824

Bruno R., Carbone V., 2013, *Living Reviews in Solar Physics*, **10**, 2

Chen C. H. K., et al., 2020, *ApJS*, **246**, 53

Chhiber R., 2018, PhD thesis, University of Delaware

Chhiber R., Ruffolo D., Matthaeus W. H., Usmanov A. V., Tooprakai P., Chuychai P., Goldstein M. L., 2021, *ApJ*, **908**, 174

Chhiber R., Attie R., Matthaeus W. H., Roy S., Thompson B. J., 2025, *MNRAS*, **544**, 2848

Consolini G., De Marco R., Carbone V., 2015, *ApJ*, **809**, 21

Cuesta M. E., et al., 2022, *The Astrophysical Journal Letters*, **932**, L11

Davis N., et al., 2023, *ApJ*, **950**, 154

Deforest C., et al., 2022, in 2022 IEEE Aerospace Conference. pp 1–11, doi:10.1109/AERO53065.2022.9843340

Dmitruk P., Matthaeus W. H., 2007, *Phys. Rev. E*, **76**, 036305

Dmitruk P., Mininni P. D., Pouquet A., Servidio S., Matthaeus W. H., 2011, *Phys. Rev. E*, **83**, 066318

Dmitruk P., Mininni P. D., Pouquet A., Servidio S., Matthaeus W. H., 2014, *Phys. Rev. E*, **90**, 043010

Dutta P., Horn P. M., 1981, *Reviews of Modern Physics*, **53**, 497

Feynman J., Ruzmaikin A., 1994, *J. Geophys. Res.*, **99**, 17645

Frisch U., Pouquet A., Leorat J., Mazure A., 1975, *Journal of Fluid Mechanics*, **68**, 769

Hathaway D. H., 2015, *Living Reviews in Solar Physics*, **12**, 4

Huang Z., et al., 2023, *ApJ*, **950**, L8

Huang Z., Velli M., Chandran B. D. G., Shi C., Ding Y., Matteini L., Choi K.-E., 2025, *ApJ*, **990**, L34

Hwa T., Kardar M., 1992, *Phys. Rev. A*, **45**, 7002

Isaacs J. J., Tessein J. A., Matthaeus W. H., 2015, *Journal of Geophysical Research (Space Physics)*, **120**, 868

Klein K. G., et al., 2023, *Space Sci. Rev.*, **219**, 74

Korzeniowska M. A., Theodorsen A., Rypdal M., Garcia O. E., 2023, *Physical Review Research*, **5**, L022066

Lamarre H., Charbonneau P., Noraz Q., Strugarek A., Blaise A., Brun A. S., Carlsson M., Gudiksen B. V., 2025, *Phys. Rev. E*, **112**, L063202

Levine R. H., Altschuler M. D., Harvey J. W., 1977, *J. Geophys. Res.*, **82**, 1061

Machlup S., 1981, in Sixth International Conference on Noise in Physical Systems. National Bureau of Standards, Wash. DC, pp 157–160

Matthaeus W. H., Goldstein M. L., 1982a, *J. Geophys. Res.*, **87**, 6011

Matthaeus W. H., Goldstein M. L., 1982b, *J. Geophys. Res.*, **87**, 10347

Matthaeus W. H., Goldstein M. L., 1986, *Phys. Rev. Lett.*, **57**, 495

Matthaeus W. H., Dasso S., Weygand J. M., Milano L. J., Smith C. W., Kivelson M. G., 2005, *Phys. Rev. Lett.*, **95**, 231101

Matthaeus W. H., Breech B., Dmitruk P., Bemporad A., Poletto G., Velli M., Romoli M., 2007, *ApJ*, **657**, L121

Matthaeus W. H., Pouquet A., Mininni P. D., Dmitruk P., Breech B., 2008, *Phys. Rev. Lett.*, **100**, 085003

McComas D. J., others 2008, Solar Probe Plus: Report of the Science and Technology Definition Team. National Aeronautics and Space Administration, Goddard Space Flight Center, Greenbelt, MD

McComas D. J., et al., 2025, *Space Sci. Rev.*, **221**, 100

Moffatt H. K., 1969, *Journal of Fluid Mechanics*, **35**, 117

Montroll E. W., Shlesinger M. F., 1982, *Proceedings of the National Academy of Science*, **79**, 3380

Nakagawa Y., Levine R. H., 1974, *ApJ*, **190**, 441

Ponty Y., Politano H., Pinton J.-F., 2004, *Phys. Rev. Lett.*, **92**, 144503

Pradha R. A., Roy S., Matthaeus W. H., Wang J., Chhiber R., Pecora F., Yang Y., 2025, *ApJ*, **984**, L23

Priest E. R., Heyvaerts J. F., Title A. M., 2002, *ApJ*, **576**, 533

Ruiz M. E., Dasso S., Matthaeus W. H., Weygand J. M., 2014, *Sol. Phys.*, **289**, 3917

Servidio S., Matthaeus W. H., Wan M., Ruffolo D., Rappazzo A. F., Oughton S., 2014, *ApJ*, **785**, 56

Sharma R., Morton R. J., 2023, *Nature Astronomy*, **7**, 1301

Smith C. W., L’Heureux J., Ness N. F., Acuña M. H., Burlaga L. F., Scheifele J., 1998, *Space Sci. Rev.*, **86**, 613

Stone E. C., Frandsen A. M., Mewaldt R. A., Christian E. R., Margolies D., Ormes J. F., Snow F., 1998, *Space Sci. Rev.*, **86**, 1

Van Der Ziel A., 1950, *Physica*, **16**, 359

Velli M., Grappin R., Mangeney A., 1989, *Phys. Rev. Lett.*, **63**, 1807

Wang J., Matthaeus W. H., Chhiber R., Roy S., Pradella R. A., Pecora F., Yang Y., 2024a, *Sol. Phys.*, **299**, 169

Wang J., et al., 2024b, *ApJ*, **967**, 150

Wang J., Pecora F., Chhiber R., Roy S., Matthaeus W. H., 2026, *Proceedings of the National Academy of Science*, **123**, e2519811122

Zhou Y., Matthaeus W. H., Roberts D. A., Goldstein M. L., 1990, *Phys. Rev. Lett.*, **64**, 2591

## APPENDIX A: GENERATION OF SYNTHETIC DATA

We first give a basic overview of our discrete Fourier transform and power spectral density formalism. Suppose the discrete, bounded time series we wish to generate is represented by  $x_j$  on the time grid  $t_j = j\Delta t$ ,  $j = 0, \dots, N-1$ , over the time domain  $[0, T]$  where  $T = N\Delta t$ . Let  $X_m$  be the discrete Fourier transform of  $x_j$  on the frequencies  $f_m$ , so

$$X_m = \Delta t \sum_{j=0}^{N-1} e^{-i2\pi m j / N} x_j, \quad (\text{A1})$$

$$f_m = \frac{m}{N\Delta t}, \quad m = -\frac{N}{2} + 1, \dots, \frac{N}{2}. \quad (\text{A2})$$

The power spectral density  $S_m$  is related to  $X_m$  by  $S_m = \langle X_m^* X_m \rangle / T$  under the constraint that  $\tau_c \ll T$ , where the asterisk stands for taking the complex conjugate. By Hermitian symmetry,  $X_m = X_{-m}^*$ .

We now construct the discrete, normalized power spectrum:

$$S_m = \frac{1}{C} \begin{cases} 0 & f_m = 0 \\ 1 & 0 < |f_m| < f_{\text{break}} \\ \left(\frac{f_m}{f_{\text{break}}}\right)^{-\alpha} & |f_m| \geq f_{\text{break}} \end{cases} \quad (\text{A3})$$

where

$$C = \frac{1}{N\Delta t} \left[ \left( \frac{1}{2\Delta t f_{\text{break}}} \right)^{-\alpha} + 2 \lfloor N\Delta t f_{\text{break}} \rfloor + 2 \sum_{m=\lfloor N\Delta t f_{\text{break}} + 1 \rfloor}^{N/2-1} \left( \frac{m}{N\Delta t f_{\text{break}}} \right)^{-\alpha} \right], \quad (\text{A4})$$

where  $-\alpha < -1$  is the power-law index. Note that the constraint of  $S_0 = 0$  ensures  $\langle x_j \rangle = 0$ , and the normalization ensures  $\langle x_j^2 \rangle = 1$ . Note also that when calculating the normalization constant, an integration of equation A3 instead of a summation as in equation A4 is feasible, where the result is  $C = 2f_{\text{break}} [\alpha/(\alpha + 1)]$ . But this leads to numerical errors due to the discreteness of the spectrum.

Now,  $S_m$  is real by definition while  $X_m$  may not be, and  $|X_m| = (TS_m)^{1/2}$ . Thus we assign uniformly distributed random phases  $\phi_m$  to each  $|X_m|$ , with  $\phi_m \in [0, 1]$  and  $\phi_{N/2} \equiv 1$  since  $X_{N/2}$ , the amplitude at the Nyquist frequency, must be real. So  $X_m$  takes the form

$$X_m = \left( \frac{T}{C} \right)^{1/2} \begin{cases} 0 & f_m = 0 \\ e^{i2\pi\phi_m} & 0 < f_m < f_{\text{break}} \\ e^{i2\pi\phi_m} \left( \frac{f_m}{f_{\text{break}}} \right)^{-\alpha/2} & f_m \geq f_{\text{break}} \end{cases} \quad (\text{A5})$$

for the positive frequencies with  $m = 0, \dots, N/2$ , and  $X_{-m} = X_m^*$  for the negative frequencies with  $m = -N/2 + 1, \dots, -1$ .

Finally, the random time series  $x_j$  can be constructed by inverse discrete Fourier transforming  $X_m$ :

$$x_j = \frac{1}{N\Delta t} \sum_{m=-N/2+1}^{N/2} e^{i2\pi m j / N} X_m, \quad (\text{A6})$$

$$t_j = j\Delta t, \quad j = 0, 1, \dots, N-1. \quad (\text{A7})$$

Eqs. A1 and A6 apply for any Fourier transform pairs.

This paper has been typeset from a *TeX/LaTeX* file prepared by the author.